Research Square

Preprints are preliminary reports that have not undergone peer review.
They should not be considered conclusive, used to inform clinical practice,
or referenced by the media as validated information.

Spatially Decoupled Polar Vortices and Ferromagnetism in Gate-Tunable Twisted Bilayer PbO

Keying Han
Yanshan University
Yajing Liu
Yanshan University
Peipei Xue
Yanshan University
Yanyan Wan
Yanshan University
Yinglun Sun
Yanshan University
Shenghan Shi
Yanshan University
Biao Ma
Yanshan University
Mengyu Zhou
Yanshan University
Chaofeng Gao
Yanshan University
Bochong Wang
Yanshan University
Congpu Mu
Yanshan University
Yingchun Cheng
iamyccheng@ysu.edu.cn
Yanshan University

Article

Keywords:

Posted Date: November 24th, 2026

DOI: https://doi.org/10.21203/rs.3.rs-11722668/v1

License: This work is licensed under a Creative Commons Attribution 4.0 International License.
Read Full License

Additional Declarations: No competing interests reported.

Spatially Decoupled Polar Vortices and Ferromagnetism in Gate-Tunable Twisted Bilayer PbO

Keying Han[1], Yajing Liu[1], Peipei Xue[1], Yanyan Wan[1], Yinglun Sun[1], Shenghan Shi[1], Biao Ma[1], Mengyu Zhou[1], Chaofeng Gao[1], Bochong Wang[1], Congpu Mu[1], Yingchun Cheng[1,*]

[1]Key Laboratory for Microstructural Material Physics of Hebei Province, School of Science, Yanshan University, Qinhuangdao, 066004, China

[*]**Author to whom correspondence should be addressed:**

iamyccheng@ysu.edu.cn

Abstract

Two-dimensional multiferroics are fundamentally constrained by the chemical incompatibility between polarization and magnetic order. Moiré superlattices avoid this limit by generating polarization through interlayer twisting, yet coexisting and tunable magnetic order remains an open challenge. Here, using non-polar, non-magnetic α-PbO as a model system, we propose a strategy for spatially decoupling polarization and magnetism in a Lieb moiré superlattice under hole doping. First-principles calculations show that the chiral in-plane polar vortices emerge within AA stacking regions. Further, the out-of-plane polarization (up to 34.9 pC/m at θ_t = 36.87°) yields a periodic electrostatic potential, forming a programmable polar substrate for adjacent material tuning. Flat bands with a narrow bandwidth of 3.2 meV localize within the AC stacking regions at θ_t = 10.39°. The resulting van Hove singularity triggers a Stoner instability, inducing ferromagnetism upon hole doping. Polarization and magnetism localize to distinct stacking domains and can be regulated by electric gating. These findings provide opportunities for designing high-density, multifunctional memory in low-dimensional systems.

Introduction

Research on multiferroic phases in two-dimensional (2D) systems represents a core direction for advancing high-density, low-power information storage technologies[1-8]. The key challenge lies in achieving synergistic control of multiple degrees of freedom, such as polarization and magnetism, within a single material, thereby enabling multi-state information encoding that transcends the limits of conventional binary systems[7,9]. However, the realization of intrinsic polarization and magnetism in these low-dimensional systems is fundamentally constrained by a well-known chemical exclusion rule. Conventional ferroelectricity typically requires cations with an empty *d* electronic configuration, whereas the emergence of magnetic order necessitates transition metal ions with partially filled *d* orbitals[10,11]. This intrinsic competition between polarization and magnetic orders presents a significant and long-standing challenge in the design of multifunctional materials[2,12,13].

Twistronics provides a new physical paradigm where polarization no longer relies on intrinsic chemical bonding, but is instead induced by the breaking of spatial inversion symmetry through interlayer twisting[14-19]. Owing to the periodic stacking domains in the moiré superlattice, spatially decoupled local polarization emerges naturally[20-23]. However, achieving stable magnetic order coexisting with the emergent polarization while ensuring flexible tunability remains a pivotal obstacle in such moiré superlattices. Current strategies for designing moiré ferromagnetism rely on either twisting existing magnetic layers or introducing magnetic dopants[24-28]. These approaches yield either magnetic states with limited tunability or extrinsic chemical disorder that disrupts the periodicity of the moiré polarization field and magnetic order.

The unique stereochemical activity of Pb 6s lone pairs in α-PbO induces significant interlayer interactions, making it an excellent candidate for moiré engineering. In this work, using non-polar, non-magnetic α-PbO as a model system, we propose a mechanism for the spatial decoupling of polarization and magnetism in the moiré superlattice under hole doping. Our first-principles calculations reveal that the spatially heterogeneous reconstruction of the moiré superlattice is driven by the significant generalized stacking fault energy (GSFE). In AA stacking regions with weak

repulsion, the differential sublayer relaxation breaks inversion symmetry, spontaneously establishing an in-plane (IP) chiral polarization vortex. Conversely, in AC stacking regions featuring strong repulsion, electrons are localized into narrow flat bands, with the bandwidth collapsing to 3.2 meV at a twist angle (θ_t) of 10.39°. The resulting van Hove singularities trigger a Stoner instability, inducing magnetism via hole doping. Magnetic moments and polarization emerge in distinct stacking domains of the moiré superlattice, leading to spatial separation of the two order parameters, i.e., spatial decoupling. Moreover, both polarization and magnetism can be regulated electrically, providing a viable platform for tunable multi-state memory operations. The moiré superlattice further reaches an areal density of 1.01×10^{17} m^{-2} (θ_t = 10.39°), highlighting its potential for high-density information storage. The out-of-plane (OOP) polarization reaches a maximum of 34.9 pC/m and gives rise to a long-range periodic electrostatic potential, rendering the system a programmable polar substrate for modulating adjacent materials. This work elucidates the magnetic mechanism induced by hole doping in moiré systems and provides a design paradigm for low dimensional systems with spatially decoupled polarization and magnetism.

Results

Crystal structures of untwisted bilayer PbO

Bulk α-PbO, which has been successfully synthesized experimentally, is stable under ambient conditions, and monolayers can be mechanically exfoliated from it[29,30]. Monolayer α-PbO crystallizes in a Lieb lattice with the space group P4/nmm with lattice constant of 4.07 Å. As illustrated in **Fig. 1a**, the monolayer features a central oxygen layer sandwiched between two Pb atomic planes, where each O atom is tetrahedrally coordinated to four Pb atoms. The Pb^{2+} cation features a $6s^2$ lone pair configuration after losing its two 6p valence electrons. Because the strong electronegativity of oxygen combined with relativistic effects induces significant hybridization between the O 2p and Pb 6s orbitals, the Pb^{2+} $6s^2$ lone pair electrons present evident stereoelectronic activity (right panel of **Fig. 1a**)[31,32]. The lone pair plays a key role in interlayer interactions in bilayer PbO because of outward extension. To elucidate the interlayer interactions governed by different stacking sequences in bilayer

PbO, we analyze the electron localization function (ELF) of three typical configurations, including AA, AB/BA, and AC **(Fig. 1b)**. The AA configuration represents a direct vertical alignment of the top and bottom monolayers. The AB and BA sequences are symmetrically equivalent, involving the shift of $0.5a_0$ along the x or y direction, respectively. In contrast, the AC stacking corresponds to a diagonal displacement of ($0.5a_0$, $0.5a_0$), vertically aligning the Pb atoms across layers. The different stacking configurations result in different interlayer electron localization reflected by ELF. Note that the ELF increases monotonically with the degree of electron localization, ranging from completely delocalized to fully localized electronic states. The AC stacking exhibits high ELF, indicating that vertical Pb-Pb alignment induces strong interlayer electron localization and repulsion. In contrast, AA stacking shows significantly lower ELF values, reflecting weak interlayer coupling, while AB/BA configurations present intermediate characteristics. Such differences in electronic interactions directly dictate the stacking energy landscape, which is manifested as the GSFE of the bilayer PbO (**Fig. 1c)**. Due to the strong repulsion induced by highly localized electrons between the head-to-head Pb lone pairs at the interface, the AC configuration has the highest energy. The lowest GSFE value is found for the AA stacking, where the offset atomic arrangement reduces interlayer repulsion, leading to thermodynamic stability. Accordingly, the GSFE increases in the order AA, AB/BA, and AC.

IP displacement and polar vortex in twisted bilayer PbO (tb-PbO)

Building upon the distinct stacking configurations, we construct the tb-PbO (Supplementary Note 1). The tb-PbO with angle of $\theta_t = 10.39°$ is presented in **Fig. 2a**, where AA, AB/BA, and AC stacking regions can be observed in the moiré superlattice. There are 6 sublayers of tb-PbO, which are labeled L1 to L6. Due to the inherent energy difference among these regions, a spontaneous lattice reconstruction occurs in the moiré superlattice. The stacking-dependent GSFE drives the lattice reconstruction, presenting a complex topological texture in the tb-PbO. We visualize the atomic reconstruction by mapping the atomic displacement vector $\Delta\mathbf{r} = \mathbf{r}_{relaxed} - \mathbf{r}_{ini}$, where $\mathbf{r}_{relaxed}$ and $\mathbf{r}_{ini}$ represent the positions after relaxation and the initial positions, respectively. The $\Delta\mathbf{r}$ of the six layers of the tb-PbO with $\theta_t = 10.39°$ is extracted after relaxation, and the results

are depicted in **Fig. 2b**. The magnitude of $\Delta\mathbf{r}$ exhibits a strong stacking dependence, following the order $\Delta\mathbf{r}_{AC} > \Delta\mathbf{r}_{AB} > \Delta\mathbf{r}_{AA}$. The visible lattice relaxation in AC regions stems from the strong thermodynamic driving force. The vortex displacement vectors form a network within the 2D plane, where the upper (L1-L3) and lower (L4-L6) sublayers arrange into clockwise and counterclockwise vortices, respectively. Therefore, the displacement field of the moiré superlattice shows spontaneous symmetry breaking, evolving into a distinct chiral vortex state. Furthermore, the paired vortex structures (L1, L6), (L2, L5), and (L3, L4) exhibit opposite chirality. Such chiral vortex displacement patterns persist across all twist angles (Supplementary Note 2).

The vortex reconstruction of cations (Pb) and anions (O) fundamentally breaks the centrosymmetry of the tb-PbO, generating a robust polarization. To quantify this effect, we evaluated the local polarization field **P** using the Born effective charge tensor (Z*), calculated as $\boldsymbol{p}_i = \frac{e}{\Omega_c} \omega_j \mathbf{Z}_j^* \boldsymbol{u}_j$[33]. Given the symmetric Pb-O-Pb configuration of PbO, we employed the smallest unit consisting of each O atom and its eight nearest neighbors to characterize the polarization of the top and bottom layers (see Supplementary Note 3 for details). **Figure 2c** presents the IP polarization texture for the θ_t = 10.39° superlattice. The maximum local polarization reaches approximately 9.20 pC/m, which surpasses the polarization magnitudes reported for conventional sliding ferroelectrics (e.g., MoS_2)[34]. Quantitative analysis of the polarization reveals a localization pattern where the chiral polarization vortices are concentrated at the AA stacking sites, distinct from the displacement maxima at AC sites. This is reasonable because AC regions exhibit large displacements in each sublayer, but the Pb and O sublayers move almost in phase, resulting in a cancellation of the net dipole moment. Conversely, there is a significant differential displacement in the AA regions. The differential offset effectively separates the cationic and anionic centers, thereby yielding the observed polarization peaks at the AA stacking sites.

The IP displacement fields and local polarization distributions within tb-PbO under various twist angles are evaluated (Supplementary Notes 2 and 4). **Figures 2d, e** illustrate the evolution of their respective maxima as a function of θ_t. Specifically, the

maximum displacement vector across the three sublayers exhibits a non-uniform behavior as it initially decreases with increasing θ_t up to 22.62°, followed by a subsequent increase up to 36.87° **(Fig. 2d)**. Driven by the enhanced independent evolution among the sublayers that governs the polarization, the maximum IP polarization of the moiré superlattice increases with increasing θ_t **(Fig. 2e)**. Specifically, the IP vortex polarization culminates in a maximum value of 22.4 pC/m at the largest twist angle of 36.87°.

Interlayer distance and OOP polarization of the tb-PbO

The different stacking distribution in moiré superlattices triggers local atomic reconstruction and spatially dependent vertical lattice expansion. The head-to-head arrangement of interlayer Pb atoms in the AC stacking region induces strong repulsion, leading to the maximum interlayer distance within the moiré superlattice **(Fig. 3a)**. The large interlayer distance implies the interlayer electronic coupling reduction, which in turn results in a significant decrease of charge transfer in the AC region relative to the AA and AB stacking domains **(Fig. 3b)**. Furthermore, the interlayer charge transfer increases as the θ_t decreases, implying that the interlayer coupling strength is enhanced at smaller θ_t (Supplementary Note 5).

For the moiré superlattice with a twist angle of 10.39°, the interlayer distance exhibits periodic spatial modulation ranging from 2.81 to 3.98 Å, inducing periodic OOP polarization in the upper layer with amplitudes ranging from -15.10 to 10.70 pC/m (**Figs. 3c, d)**. Similar moiré periodicity in OOP polarization is observed across different θ_t (Supplementary Note 6). Because of the significantly enhanced differences among OOP displacement vectors of the three sublayers, the maximum OOP polarization increases monotonically with θ_t, which is consistent with the evolution of IP polarization (**Figs. 3e, f)**. The tb-PbO exhibits a large OOP polarization of 34.9 pC/m at θ_t = 36.87°, which surpasses values reported in other 2D ferroelectrics, such as α-In_2Se_3 and $CuInP_2S_6$[34-38]. The OOP polarization is achieved through the interplay between moiré engineering and stacking-dependent inhomogeneous interlayer interactions. Consequently, a long range ordered electrostatic potential field, characterized by the moiré superlattice periodicity, emerges on the material surface. As

shown in **Fig. 3g**, the surface electrostatic potential at 3 Å above the top Pb atomic surface exhibits a decreasing trend following the sequence of AA, AB, and AC stacking regions. Stacking-induced interfacial charge redistribution results in a moiré periodic modulation of surface potential. Since similar periodic potential fields are universal across different twist angles (Supplementary Note 7), moiré engineering offers a continuously tunable, long range surface electrostatic potential. Therefore, the tb-PbO can be utilized as an ideal polar substrate for precisely modulating the electronic states of adjacent 2D quantum materials.

Moiré flat bands and doping-induced ferromagnetism in tb-PbO

To elucidate the electronic properties of the moiré superlattice, we calculated the band structures of tb-PbO with different θ_t. While the valence band remains highly dispersive at the maximum twist angle of 36.87°, a distinct flat band is observed at 22.62° (**Fig. 4a** and Supplementary Note 8**)**. The flat band states are strongly localized in AC stacking regions and consist predominantly of O 2p orbitals, with a minor Pb 6s contribution **(Figs. 4b-d)**. This observable spatial confinement mirrors lattice reconstruction, establishing a strong correlation between structural vortex patterns and localized electronic states. **Figure 4e** shows that the bandwidth narrows progressively with decreasing θ_t. Remarkably, the bandwidth shrinks to 3.2 meV at the θ_t of 10.39°. This value is significantly smaller than those observed in conventional small angle moiré systems (e.g., $BaTiO_3$, MoS_2, and graphene)[20,39,40], indicating the onset of strong electronic correlation effects in this system. The valence band structure of tb-PbO exhibits a distinctive Mexican hat dispersion near the Γ point (**Fig. 4f)**. The flat band and Mexican hat dispersion induce a sharp van Hove singularity in the density of states (DOS) (**Fig. 4c)**. Although tb-PbO is intrinsically non-magnetic, due to the van Hove singularity near the Fermi level, the strong exchange-driven spin splittings can be induced by hole doping (**Fig. 4g)**[41]. Specifically, at a hole concentration of 14.17×10^{13} cm^{-2}, time-reversal symmetry is broken, resulting in a significant exchange splitting of the spin bands near the Fermi level. When the hole concentration increases to 21.25×10^{13} cm^{-2}, the net magnetic moment saturates at a maximum value of 2.13 μ_B. This evolutionary pathway of ferromagnetism driven by hole doping consistently applies to

tb-PbO systems with different twist angles (Supplementary Note 9). **Figure 4h** demonstrates that hole doping effectively breaks the spin degeneracy, inducing a spontaneous ferromagnetic phase transition. The physical origin of this magnetism is validated via the Stoner criterion, where $I \times DOS(E_F) > 1$[42-44]. Here, $DOS(E_F)$ denotes the DOS per atom per spin at the Fermi level for the nonmagnetic state, and I is the exchange interaction parameter. It can be expressed as $I = \Delta/M$, where M is the magnetic moment per atom (in units of μ_B) and Δ is the energy of band splitting. At a hole concentration of 14.17×10^{13} cm^{-2}, the calculated $I \times DOS(E_F) = 3.53 > 1$ explicitly satisfies the Stoner criterion, confirming that the emergence of ferromagnetism is driven by Stoner instability inherent to the flat bands.

Spatial separation of polarization and ferromagnetism in hole-doped tb-PbO

It should be noted that the spatial distribution of this moiré magnetism exhibits stacking dependence, with magnitudes decreasing in the order of AC, AB, and AA (**Fig. 5a)**. The magnetic moments in the top and bottom layers follow exactly the same spatial distribution and stacking-dependent trend (Supplementary Note 10). Such heterogeneous distribution stems directly from the real-space localization of moiré flat bands. As previously noted, strong interlayer repulsion in the AC stacking region drives a lattice reconstruction that localizes the predominantly O 2p derived flat band states. Consequently, when hole doping leads to Fermi level shift at the van Hove singularity, Stoner instability becomes evident in the AC regions, resulting in spin splitting and establishing moiré magnetism.

To assess the energetic preference of the magnetic orientation, we calculated the magnetic anisotropy energy (MAE) as a function of hole doping concentration (**Fig. 5b)**. The MAE is defined as the energy difference between IP and OOP magnetization configurations, given by $MAE = E(\parallel) - E(\perp)$[45]. The twisted system maintains an IP easy magnetization under hole doping. Within the hole doping concentration of 23.61×10^{13} cm^{-2}, the MAE reaches a peak value of approximately -0.16 meV per moiré superlattice. Furthermore, hole doping in the twisted system not only induces magnetism but also significantly modifies the lattice degrees of freedom and polarization behavior (**Fig. 5c)**. We clearly observe that the maximum IP polarization

increases monotonically with hole doping concentration, whereas the OOP polarization exhibits a non-linear evolution characterized by an initial decrease followed by a rebound. Therefore, both the magnetic and polarization degrees of freedom of the system can be regulated under hole doping.

By applying dual-gate voltages, hole carriers can be injected into the tb-PbO (**Fig. 5d)**. Spatial decoupling is observed within the moiré superlattice, where chiral polar vortices are mainly distributed in the AA regions, while ferromagnetic moments are concentrated in the AC regions (**Fig. 5e**). Such spatial coexistence and separation of polarization and magnetism offer the possibility of dual-channel information encoding within a single moiré supercell. Under gate-tunable hole doping, both the polarization amplitude and the magnetic moment can be continuously modulated, offering the possibility of multi-state storage configurations. Notably, the areal density estimate here is based on the geometric size of the moiré unit cell. Taking tb-PbO with a θ_t of 10.39° as an example, its areal density reaches 1.01×10^{17} m^{-2}, corresponding to a pixel density of 64.9 Tb/in^2, highlighting the practical potential of this system for high-density information storage.

Conclusions

In summary, we propose a paradigm to achieve polarization and ferromagnetism with spatial decoupling in a moiré system. By utilizing tb-PbO as a model system, we found that the repulsion arising from Pb 6s lone pairs and the significant GSFE drive spatial lattice reconstruction. In AA stacking regions, lattice relaxation induces a network of IP chiral polar vortices. In contrast, in AC stacking regions where lone pairs face each other, strong localized electrons induce narrow flat bands, with a bandwidth of 3.2 meV for tb-PbO at $\theta_t = 10.39°$. The resulting van Hove singularity drives Stoner instability, inducing ferromagnetism via hole doping. Such polar vortices and magnetism are not only spatially decoupled but can also be regulated by a dual-gate device. Moreover, the long-range electrostatic field created by the OOP polarization also suggests that this system is a natural programmable substrate for controlling low-dimensional quantum states. Our findings reveal that moiré engineered spatial

decoupling provides an exciting opportunity for designing high density multi state memories.

Methods

DFT Settings

The first-principles calculations were performed using the DS-PAW software based on the projected augmented wave (PAW) plane-wave basis set[46-48]. Electronic exchange and correlation interactions were described using the Perdew-Burke-Ernzerhof (PBE) functional within the generalized gradient approximation (GGA)[49,50]. To minimize interaction between periodic images, a vacuum space exceeding 15 Å was applied, and a plane-wave cut-off energy of 400 eV was utilized. For Brillouin zone sampling, the Monkhorst-Pack method was employed. Specifically, a 15×15×1 mesh was adopted for the optimization of monolayer and bilayer geometries, whereas a 2×2×1 mesh was used for twisted configurations. The convergence criteria were 0.05 eV $Å^{-1}$ for force on each atom and 1×10^{-4} eV for total energy. Additionally, the DFT-D3 correction was used to account for interlayer van der Waals interaction[51,52]. Spin-orbit coupling (SOC) effect was taken into account in the calculations of magnetic anisotropy energy (MAE).

Acknowledgements

This work was supported by the National Natural Science Foundation of China (62274087) and the Hebei Natural Science Foundation (E2025203224).

Author Contributions

Y.C.C. supervised and conceived the project. K.Y.H. wrote the manuscript and analyzed data. Y.J.L., Y.L.S. and M.Y.Z. performed the calculations. S.H.S., P.P.X. and Y.Y.W. prepared some diagrams. Y.J.L., M.Y.Z. and B.M. contributed to investigation. C.F.G, C.P.M. and B.C.W were responsible for project administration. All authors reviewed the manuscript before its submission.

Competing interests

The authors declare no competing interests.

Data availability

All data generated or analyzed during this study are included in this manuscript and its Supplementary Information file.

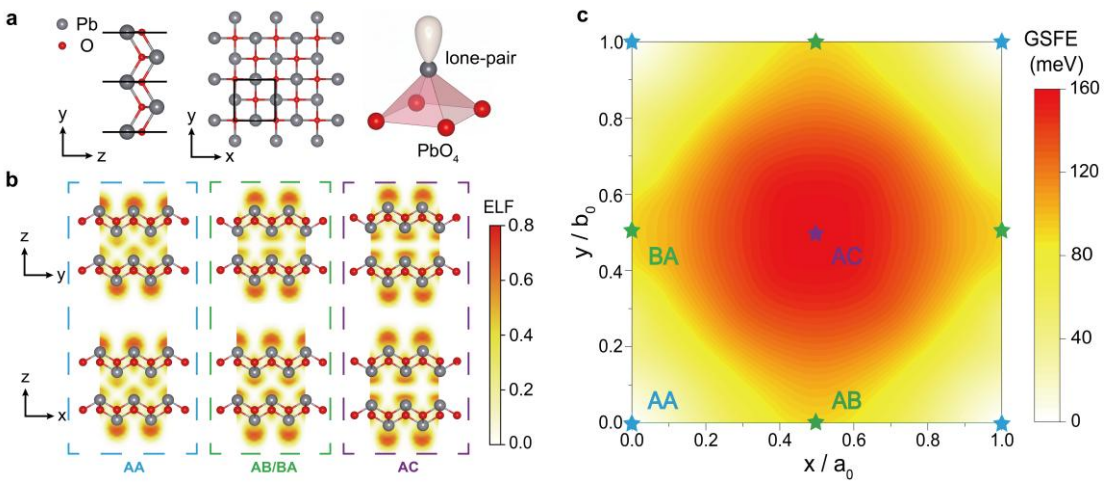


Fig. 1 | Structures of untwisted bilayer PbO. a Side and top views of monolayer PbO, and the schematic diagram of lone-pair for PbO_4 tetrahedron. **b** Side views of ELFs for bilayer PbO with AA, AB/BA, and AC stacking configurations. **c** GSFE of bilayer PbO.

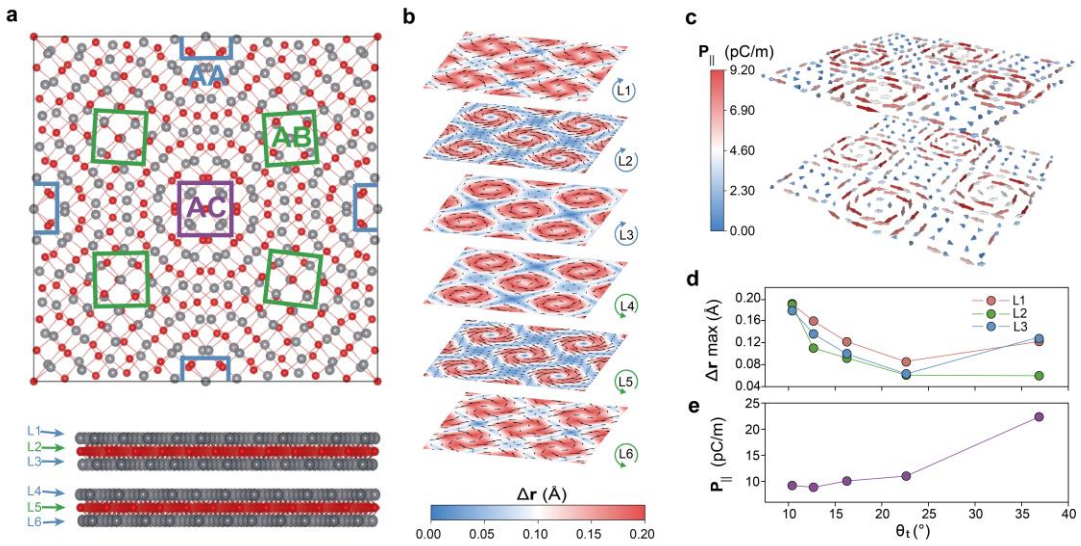


Fig. 2 | IP displacement and polar vortex in the tb-PbO. a Top and side views of the moiré superlattice with θ_t = 10.39F. The AC, AB, and AA stackings in the moiré superlattice are marked in purple, green, and blue, respectively. **b** IP displacement fields of the six sublayers at θ_t = 10.39°. **c** IP vortex polarization patterns in tb-PbO at θ_t = 10.39°. $\mathbf{P}_{\parallel}$ denotes the IP polarization. **d** The IP max displacement and **e** polarization of the upper layer of tb-PbO as a function of θ_t.

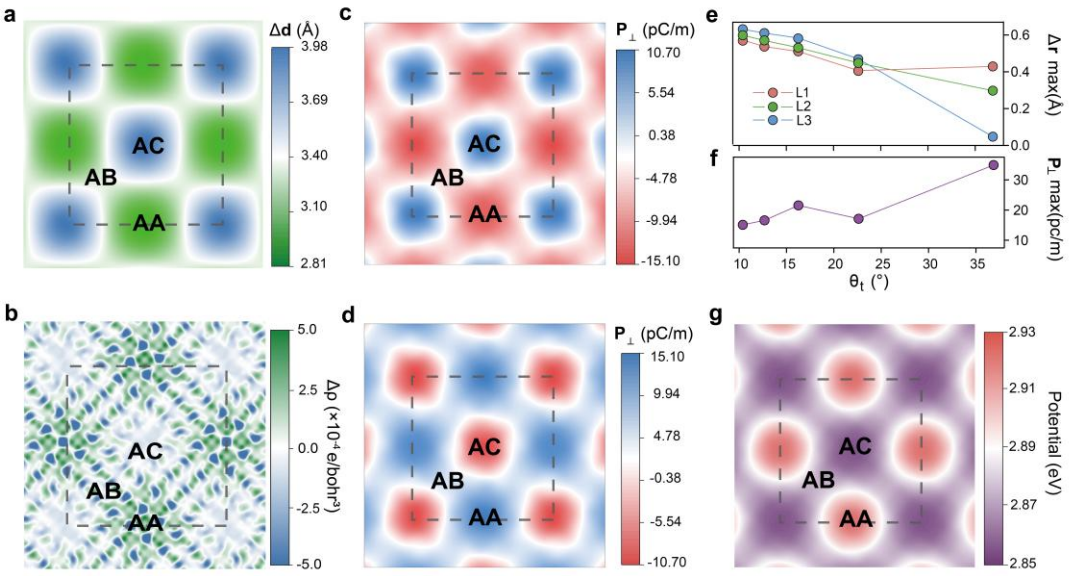
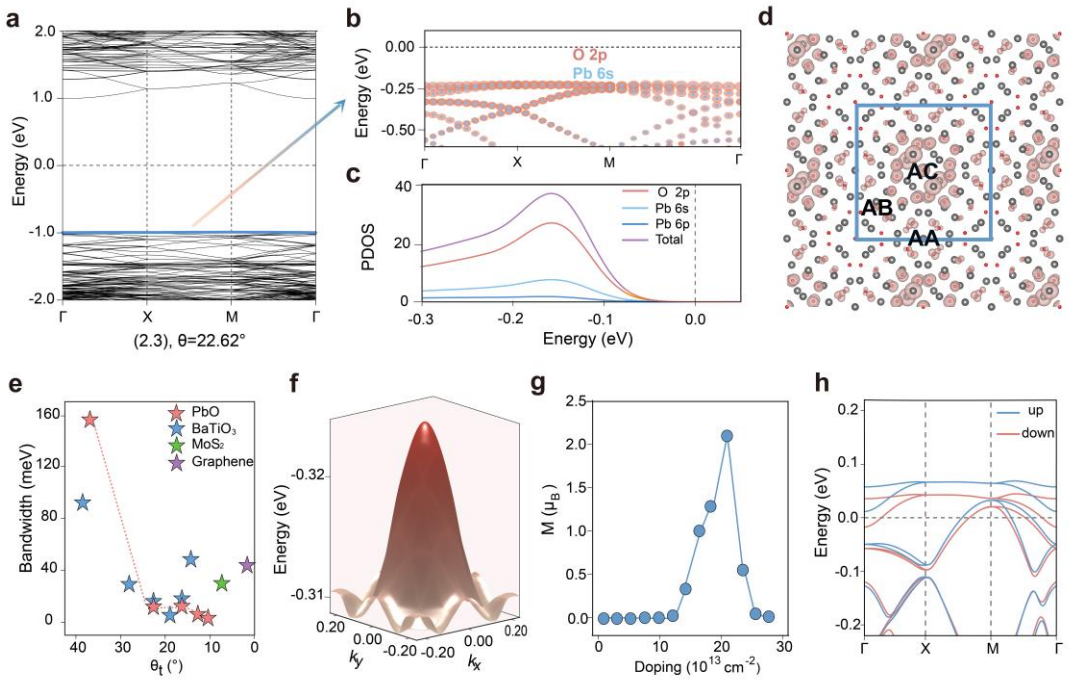


Fig. 3 | Interlayer distance and OOP polarization distribution of the tb-PbO. a Interlayer distance and **b** interlayer charge density difference in the moiré superlattice at $\theta_t = 10.39°$. The isosurface is set to 3×10^{-4} eÅ^{-3}. **c** OOP polarization distributions in the top and **d** bottom layers at $\theta_t = 10.39°$. $\mathbf{P}_\perp$ denotes the OOP polarization. The polarization orientations along [001] and [00$\bar{1}$] are determined to be positive and negative, respectively. **e** The OOP max displacement and **f** polarization of tb-PbO as a function of θ_t. **g** Surface potential profiles of $\theta_t = 10.39°$ evaluated at a distance of 3 Å from the Pb surface.



289

290 **Fig. 4 | Flat band and magnetic properties of tb-PbO under hole doping. a** Band
291 structure and **b** orbital projected band structure of tb-PbO with $\theta_t = 22.62°$. **c** Projected
292 density of states for tb-PbO. **d** The charge density of the flat band of tb-PbO at $\theta_t =$
293 22.62°. The isosurface is set to 0.0011 eÅ^{-3}. **e** Dependence of flat band bandwidth on
294 θ_t for tb-PbO and other twisted materials. **f** 3D band structure of tb-PbO with $\theta_t = 22.62°$.
295 **g** Total magnetic moment as a function of hole doping concentration. **h** Spin-resolved
296 band structure near the valence band structure for hole doping concentration of 14.17 ×
297 10^{13} cm^{-2}.

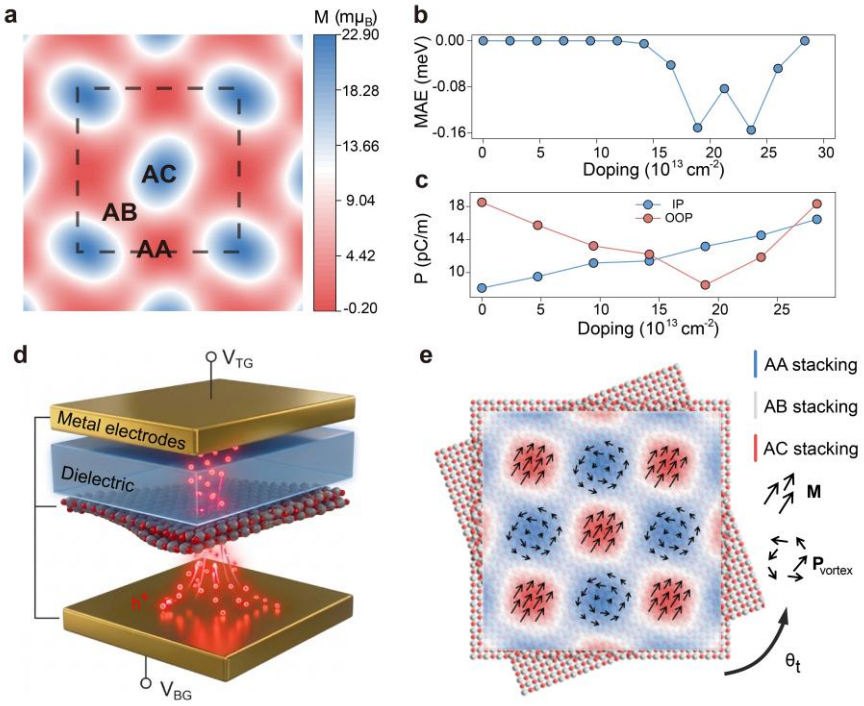


Fig. 5 | Spatial separation of polarization and ferromagnetism in tb-PbO under hole doping. a Magnetic moment distribution in tb-PbO with $\theta_t = 22.62°$ at hole doping concentration of 18.89×10^{13} cm^{-2}. **b** The MAE of tb-PbO under carrier doping. **c** The IP and OOP polarization as a function of hole doping concentration. **d** Schematic diagram of carrier doping in tb-PbO. **e** Schematic diagram of the spatial separation between the IP polar vortex and magnetic moments in tb-PbO.

References

1. Mundy, J. A. et al. Atomically engineered ferroic layers yield a room-temperature magnetoelectric multiferroic. *Nature* **537,** 523-7 (2016).
2. Spaldin, N. A. & Ramesh, R. Advances in magnetoelectric multiferroics. *Nat. Mater.* **18,** 203-212 (2019).
3. Hu, Q. et al. Ferrielectricity controlled widely-tunable magnetoelectric coupling in van der Waals multiferroics. *Nat. Commun.* **15,** 3029 (2024).
4. Xu, S. et al. Magnetoelectric coupling in multiferroics probed by optical second harmonic generation. *Nat. Commun.* **14,** 2274 (2023).
5. Mostovoy, M. J. Multiferroics: different routes to magnetoelectric coupling. *npj Spintron.* **2,** 18 (2024).
6. Feng, Y., Dai, Y., Huang, B., Kou, L. & Ma, Y. Layer Hall Effect in Multiferroic Two-Dimensional Materials. *Nano Lett.* **23,** 5367-5372 (2023).
7. Zhong, T., Li, X., Wu, M. & Liu, J. M. Room-temperature multiferroicity and diversified magnetoelectric couplings in 2D materials. *Natl. Sci. Rev.* **7,** 373-380 (2020).
8. Chen, C. et al. Emergence of Polar Vortex-Antivortex Pair Arrays in Multiferroic Superlattices. *Adv. Mater.* **38,** e01894 (2026).
9. Xie, T. et al. Tailorable multiferroic tunnel junctions from all-van der Waals multilayer stacking. *Nat. Nanotechnol.* **21,** 366-373 (2026).
10. Hill, N. Why Are There so Few Magnetic Ferroelectrics? *J. Phys. Chem. B* **104,** 6694-6709 (2000).
11. Daniel, K. Classifying multiferroics: Mechanisms and effects. *Am. Phys. Soc.* **2,** 20 (2009).
12. Eerenstein, W., Mathur, N. D. & Scott, J. F. Multiferroic and magnetoelectric materials. *Nature* **442,** 759-65 (2006).
13. Zhao, Y., Wang, Y., Yang, Y., Zhao, J. & Jiang, X. Realization of 2D multiferroic with strong magnetoelectric coupling by intercalation: a first-principles high-throughput prediction. *npj Comput. Mater.* **10,** 122 (2024).
14. Yasuda, K., Wang, X., Watanabe, K., Taniguchi, T. & Jarillo-Herrero, P. Stacking-engineered ferroelectricity in bilayer boron nitride. *Science* **372,** 1458-1462 (2021).
15. Weston, A. et al. Interfacial ferroelectricity in marginally twisted 2D semiconductors. *Nat. Nanotechnol.* **17,** 390-395 (2022).
16. Tsang, C. S. et al. Polar and quasicrystal vortex observed in twisted-bilayer molybdenum disulfide. *Science* **386,** 198-205 (2024).
17. Guo, R., Chen, H., Duan, W., Xu, Y. & Wang, C. Manipulating Charge Distribution in Moiré Superlattices by Light. *Phys. Rev. Lett.* **136,** 086903 (2026).
18. Xu, Q. et al. Engineering 2D Square Lattice Hubbard Models in 90° Twisted GeX/SnX (X =S, Se) Moiré Superlattices. *Phys. Rev. X* **15,** 041049 (2025).
19. Yang, L., Ding, S., Gao, J. & Wu, M. Atypical Sliding and Moiré Ferroelectricity in Pure Multilayer Graphene. *Phys. Rev. Lett.* **131,** 096801

(2023).
20. Lee, S., deSousa, D. J. P., Jalan, B. & Low, T. Moiré polar vortex, flat bands, and Lieb lattice in twisted bilayer $BaTiO_3$. *Sci. Adv.* **10,** eadq0293 (2024).
21. Xu, T. et al. Ultrahigh-Density Polar Vortex Lattice in Square-Shaped Moiré Bilayers of Lead Chalcogenides. *Nano Lett.* **24,** 14736-14742 (2024).
22. Sun, J., Shen, Y., Cao, T. & Liu, L.-M. Sliding and superlubric moiré twisting ferroelectric transition in HfO_2. *npj Comput. Mater.* **11,** 367 (2025).
23. Bennett, D., Chaudhary, G., Slager, R.-J., Bousquet, E. & Ghosez, P. Polar meron-antimeron networks in strained and twisted bilayers. *Nat. Commun.* **14,** 1629 (2023).
24. Xie, H. et al. Twist engineering of the two-dimensional magnetism in double bilayer chromium triiodide homostructures. *Nat. Phys.* **18,** 30-36 (2022).
25. Xu, Y. et al. Coexisting ferromagnetic-antiferromagnetic state in twisted bilayer CrI_3. *Nat. Nanotechnol.* **17,** 143-147 (2022).
26. Zhu, H. et al. Moiré-Induced Magnetoelectricity in Twisted Bilayer NiI_2. *Phys. Rev. Lett.* **135,** 196701 (2025).
27. Ye, H. & Dong, S. Magnetic and Ferroelectric Phase Diagram of Twisted CrI_3 Layers. *Phys. Rev. Lett.* **135,** 066701 (2025).
28. Tong, Q., Chen, M. & Yao, W. Magnetic Proximity Effect in a van der Waals Moiré Superlattice. *Phys. Rev. Appl.* **12,** 024031 (2019).
29. Manjunatha, U., Meher, S., Tripathi, P., Singh, A. & Ravishankar, N. Local Strain Triggers Polymorphic Phase Transformation in Layered Materials: A Case Study of Lead Oxide. *Small* **22,** e13904 (2026).
30. Ingle, A. et al. Reactive Oxygen Species Sequestration Induced Synthesis of β-PbO and Its Polymorphic Transformation to α-PbO at Atomically Thin Regimes. *ACS Nano* **16,** 10679-10691 (2022).
31. Li, F., Pan, S. & Yang, Z. Origin of second harmonic generation in noncentrosymmetric crystal structures containing lone pair electrons. *Phys. Rev. B* **112,** 125147 (2025).
32. Zhu, Z. et al. Giant Polarizability and Origin of Ferroelectricity in Layered Materials with a Litharge-Type Structural Unit. *Nano Lett.* **25,** 4093-4100 (2025).
33. Xu, T., Wang, J., Shimada, T. & Kitamura, T. Direct approach for flexoelectricity from first-principles calculations: cases for $SrTiO_3$ and $BaTiO_3$. *J. Phys.: Condens. Matter* **25,** 415901 (2013).
34. Wu, M. & Li, J. Sliding ferroelectricity in 2D van der Waals materials: Related physics and future opportunities. *Proc. Natl. Acad. Sci.* **118,** e2115703118 (2021).
35. Chi, M. et al. Emerging 2D Ferroelectric Semiconductors: From Fundamentals to Advanced Device Applications. *Adv. Sci.* **12,** e14185 (2025).
36. Li, L. & Wu, M. Binary Compound Bilayer and Multilayer with Vertical Polarizations: Two-Dimensional Ferroelectrics, Multiferroics, and Nanogenerators. *ACS Nano* **11,** 6382-6388 (2017).
37. Kruse, M. et al. Two-dimensional ferroelectrics from high throughput

computational screening. *npj Comput. Mater.* **9,** 45 (2023).
38. Zhang, C. et al. Modulation of Polarization in Sliding Ferroelectrics by Introducing Intrinsic Electric Fields. *J. Phys. Chem. Lett.* **15,** 8049-8056 (2024).
39. Kim, J. et al. Anomalous optical excitations from arrays of whirlpooled lattice distortions in moiré superlattices. *Nat. Mater.* **21,** 890-895 (2022).
40. Cantele, G. et al. Structural relaxation and low-energy properties of twisted bilayer graphene. *Phys. Rev. Res.* **2,** 043127 (2020).
41. Wang, Y. et al. Lead monoxide: a two-dimensional ferromagnetic semiconductor induced by hole-doping. *J. Mater. Chem. C* **5,** 4520-4525 (2017).
42. Janak, J. F. Uniform susceptibilities of metallic elements. *Phys. Rev. B* **16,** 255-262 (1977).
43. Seo, D. K. Density functional perturbational orbital theory of spin polarization in electronic systems. I. Formalism. *J. Chem. Phys.* **125,** 154105 (2006).
44. Sigalas, M. M. & Papaconstantopoulos, D. A. Calculations of the total energy, electron-phonon interaction, and Stoner parameter for metals. *Phys. Rev. B* **50,** 7255-7261 (1994).
45. Duan, C. G. et al. Surface magnetoelectric effect in ferromagnetic metal films. *Phys. Rev. Lett.* **101,** 137201 (2008).
46. Kresse, G. & Joubert, D. From ultrasoft pseudopotentials to the projector augmented-wave method. *Phys. Rev. B* **59,** 1758-1775 (1999).
47. Li, L. et al. Modulation of active center distance of hybrid perovskite for boosting photocatalytic reduction of carbon dioxide to ethylene. *Proc. Natl. Acad. Sci.* **121,** e2318970121 (2024).
48. Blöchl, P. E. Projector augmented-wave method. *Phys. Rev. B* **50,** 17953-17979 (1994).
49. Perdew, J. P., Burke, K. & Ernzerhof, M. Generalized Gradient Approximation Made Simple. *Phys. Rev. Lett.* **77,** 3865-3868 (1996).
50. Hammer, B., Hansen, L. B. & Nørskov, J. K. Improved adsorption energetics within density-functional theory using revised Perdew-Burke-Ernzerhof functionals. *Phys. Rev. B* **59,** 7413-7421 (1999).
51. Grimme, S., Antony, J., Ehrlich, S. & Krieg, H. A consistent and accurate ab initio parametrization of density functional dispersion correction (DFT-D) for the 94 elements H-Pu. *J. Chem. Phys.* **132,** 154104 (2010).
52. Grimme, S., Ehrlich, S. & Goerigk, L. Effect of the damping function in dispersion corrected density functional theory. *J. Comput. Chem.* **32,** 1456-1465 (2011).

Supplementary Files

This is a list of supplementary files associated with this preprint. Click to download.

- SupportingInformation.docx